filaments.

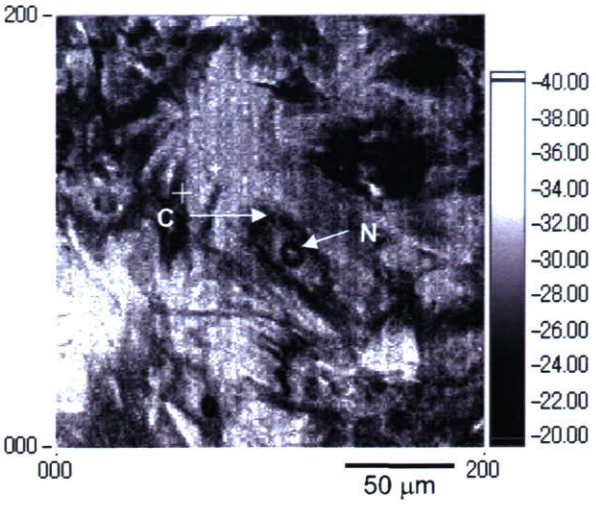

Fig. 6. Fibroblast image obtained with sound speed mode.

Fig. 7 shows the brain of rat by impedance mode. Four layers are visible; molecular layer (ML), Purkinje layer (PL), internal granular layer (IGL) and white matter (WM) in mature cerebellum. Parallel fibers in ML are axon of granule cells and play an important role in cerebella neural connection. Migrating granule cells elongate them horizontally and form a lot of excitatory synapses to dendrite of Purkinje cells. These are major neuronal circuits of cerebellum so that parallel fibers are expected to construct rich ML with development.

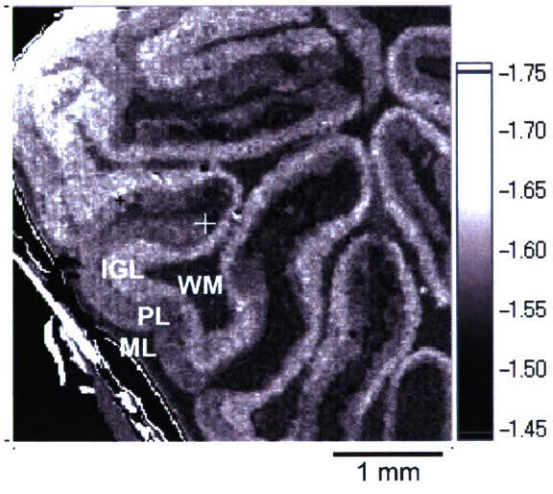

Fig. 7. Rat brain image obtained with impedance mode.

IV. Discussions

Histology has remained the acknowledged "gold standard" for cancer diagnosis or rejection diagnosis in heart transplantation because no other method has been shown to fulfill this requirement consistently. However, biopsy has some limitations and bears a small risk for the patient. For the better quality of life of patients and reducing medical cost for follow up, the method that rapidly, non-invasively and reliably identifies malignant cells or rejection-induced myocardial changes is desired. The final goal of the present study is to realize ultrasonic *in vivo* nano-imaging system that can visualize nano-scale structure of the living organ during the surgical procedure.

In order to achieve the goal, ultrasonic speed and impedance microscopy with two measurement modes was developed. Sound speed mode has been also used in the conventional scanning acoustic microscopy. An ultrasonic transducer with the frequency range up to 380 MHz was fabricated and scanning width was 100 nm to realize 800 nm resolution imaging. This imaging mode however requires the thin objects such as thinly sliced tissue or single layered cultured cells. Impedance mode was developed to break these limitations of conventional acoustic microscopy. The thin plastic plate was set upon the transducer and the image if the surface of the tissue is visualized by contacting the tissue. This mode can be applied for intra-operative histological examination at microscopic level in case the pre-operative examination cannot be performed, for example, brain surgery for treatment of epilepsy or left ventricular reduction surgery. This mechanism may also be applied for endoscopic ultrasound by miniaturizing the parts for mechanical scan.

V. Conclusions

Ultrasonic speed and impedance microscopy with two measurement modes was developed in order to develop *in vivo* imaging. The system realized high precision imaging of cells by sound speed mode and direct visualization of tissue by impedance mode. The combination of the two measurement mode would enable to measure in vivo density and other parameters useful in studies of biomechanics.

Acknowledgment

Yoshifumi Saijo thanks Dr. Sachiko Yoshida with the Toyohashi University of Technology for the experiments on rat brain.

References

[1] M. Tanaka, H. Okawai, N. Chubachi, J. Kushibiki, T. Sannomiya, "Propagation properties of ultrasound in acoustic microscopy through a double-layered specimen consisting of thin biological tissue and its holder," *Jpn J Appl Phy* 23 (1984), pp. 197-199.

[2] Y. Saijo, M. Tanaka, H. Okawai, F. Dunn, "The ultrasonic properties of gastric cancer tissues obtained with a scanning acoustic microscope system," *Ultrasound Med Biol* 17 (1991), pp. 709-714.

[3] H. Sasaki, M. Tanaka, Y. Saijo, H. Okawai, Y. Terasawa, S. Nitta, K. Suzuki, "Ultrasonic tissue characterization of renal cell carcinoma tissue," *Nephron* 74 (1996), pp. 125-130.

[4] Y. Saijo, M. Tanaka, H. Okawai, H. Sasaki, S. Nitta, F. Dunn, "Ultrasonic tissue characterization of infarcted myocardium by scanning acoustic microscopy," *Ultrasound Med Biol* 23 (1997), pp. 77-85.

[5] Y. Saijo, H. Sasaki, H. Okawai, S. Nitta, M. Tanaka, "Acoustic properties of atherosclerosis of human aorta obtained with

high-frequency ultrasound," *Ultrasound Med Biol* 24 (1998), pp. 1061-1064.

[6] Y. Saijo, H. Sasaki, M. Sato, S. Nitta, M. Tanaka, "Visualization of human umbilical vein endothelial cells by acoustic microscopy," *Ultrasonics* 38 (2000), pp. 396-399.

[7] Y. Saijo, T. Ohashi, H. Sasaki, M. Sato, C.S. Jorgensen, S. Nitta, "Application of scanning acoustic microscopy for assessing stress distribution in atherosclerotic plaque," *Ann Biomed Eng* 29 (2001), pp. 1048-53.

[8] H. Sasaki, Y. Saijo, M. Tanaka, S. Nitta, "Influence of tissue preparation on the acoustic properties of tissue sections at high frequencies," *Ultrasound Med Biol* 29 (2003), pp. 1367-72.

[9] Y. Saijo, T. Miyakawa, H. Sasaki, M. Tanaka, S. Nitta, "Acoustic properties of aortic aneurysm obtained with scanning acoustic microscopy," *Ultrasonics* 42 (2004), pp. 695-698.

[10] H. Sano, Y. Saijo, S. Kokubun, "Material properties of the supraspinatus tendon at its insertion – A measurement with the scanning acoustic microscopy," *J Musculoskeletal Res.* 8 (2004), pp. 29-34.

[11] N. Hozumi, R. Yamashita, C.K. Lee, M. Nagao, K. Kobayashi, Y. Saijo, M. Tanaka, N. Tanaka, S. Ohtsuki, "Time–frequency analysis for pulse driven ultrasonic microscopy for biological tissue characterization," *Ultrasonics* 42 (2004), pp. 717-722.

[12] N. Hozumi, A. Kimura, S. Terauchi, M. Nagao, S. Yoshida, K. Kobayashi & Y. Saijo, "Acoustic impedance micro-imaging for biological tissue using a focused acoustic pulse with a frequency Range up to 100 MHz," *Proc 2005 IEEE Int Ultrason Symp* (2005), pp. 170-173.

J Artif Organs (2007) 10:223–227
DOI 10.1007/s10047-007-0395-y

ORIGINAL ARTICLE

Hongjian Liu, PhD · Yun Luo, PhD · Masaru Higa, PhD
Xiumin Zhang, PhD · Yoshifumi Saijo, MD, PhD
Yasuyuki Shiraishi, PhD · Kazumitsu Sekine, PhD
Tomoyuki Yambe, MD, PhD

Biochemical evaluation of an artificial anal sphincter made from shape memory alloys

Abstract Severe anal incontinence is a socially incapacitating disorder and a major unresolved clinical problem that has a considerable negative impact on quality of life. In this study, we developed a new artificial anal sphincter using shape memory alloys (SMAs) in order to improve the quality of life of such patients and evaluated the influence of this sphincter on blood serum chemistry in animal experiments. The artificial anal sphincter was driven by two Ti-Ni SMA actuators sandwiching the intestine and was implanted in three female goats. Blood was collected from the jugular vein on days 1 and 4; at weeks 1 and 2; and at months 1, 2, and 3, postoperatively. Biochemical parameters including total protein, albumin, total bilirubin, aspartate aminotransferase, blood urea nitrogen, creatinine, and C-reactive protein were examined. The time courses of total bilirubin and aspartate amino transferase of the three goats were within the baseline levels after 1 week of implantation and remained normal, demonstrating no liver function complications. The blood urea nitrogen and creatinine levels remained within the normal range, indicating no renal function complications. The total protein and albumin fluctuated within the normal range throughout the duration of this study. In these goats, it was also found that the level of C-reactive protein did not increase and that there was no stricture of the intestine where the artificial sphincter was attached. Our findings indicate that the artificial sphincter SMA demonstrated no adverse influence on blood serum chemistry and exhibited an effective system performance.

Key words Shape memory alloys · Artificial anal sphincter · Biochemical evaluations · Implantation · Goat

Introduction

Severe anal incontinence (incontinence for gas, feces, or both) is a socially incapacitating disorder and a major unresolved clinical problem that has a considerable negative impact on quality of life. This condition is caused by colostomy or ileostomy, neuromuscular disorders, congenital anorectal malformation, and obstetric injury.[1] As a treatment for such patients, an artificial anal sphincter (AMS800, American Medical Systems, Minneapolis, MN, USA) was developed and has been implanted in animal models and patients. However, it has been indicated that the artificial sphincter may not withstand prolonged use because of mechanical failure and structures using a liquid drive mechanism.[1,2]

Nickel–titanium (Ni-Ti) shape memory alloys (SMAs) have many unique mechanical and material characteristics combined with good biocompatibility. SMAs are attracting considerable attention as core materials in medical applications because of their high ratio of recovery force to weight and large recoverable strains. SMAs are durable and can endure up to 50000 cycles of heating and cooling.[3,4] We have previously reported the development of artificial anal sphincters using SMAs for treating patients with neuromuscular disorders, severe congenital anomalies, or colostomy.[3,5] The artificial anal sphincter has only one deformable part and therefore has a simple structure with good durability and is expected to reduce the possibility of mechanical failure. In this study, we evaluated the influence of the artificial anal sphincter on blood serum chemistry in animal experiments.

Received: March 6, 2007 / Accepted: July 31, 2007

H. Liu (✉) · Y. Saijo · Y. Shiraishi · K. Sekine · T. Yambe
Department of Medical Engineering and Cardiology, Institute of Development, Aging and Cancer, Tohoku University, 4-1 Seiryo-machi, Aoba-ku, Sendai 980-8575, Japan
Tel. +81-22-717-8517; Fax +81-22-717-8518
e-mail: hongjianliu63@yahoo.co.jp

Y. Luo · M. Higa
Biomedical Engineering Research Organization, Tohoku University, Sendai, Japan

X. Zhang
Department of Medicine and Science in Sports and Exercise, Tohoku University Graduate School of Medicine, Sendai, Japan

Materials and methods

Animals

Three female goats weighing 50–60 kg were used. The animal experiments were performed after approval by the Research Animal Resource Committee of the Institute of Experimental Animals, Tohoku University School of Medicine, Japan.

Artificial anal sphincter device

The artificial sphincter (AS) is driven by two Ti-Ni SMA actuators sandwiching the intestine. The composition of SMA used in this study was Ti51at%Ni on an atomic basis. The actuator consists of two SMA plates ($70 \times 18.5 \times 0.7$ mm) jointed by hinges at their ends and foil type heaters attached on the SMA plates. Silicone pillows were placed on the surfaces of the SMA plates to prevent pressure concentration on the intestines, which may cause ischemia. The bilateral ends of two SMA plates of circumferential shape were fixed with latches, and the alimentary tract was placed between the two SMA actuators.

To control the opening and closing of the anal canal, two meander winding 0.2-mm wires were attached on the surface of each SMA plate as heaters. On heating, the reverse R-phase transformation occurred in the SMA plates, accompanied by shape changes from a flat shape to an arc shape. The shape change resulted in a lumen between the two SMA plates, which allowed bowel movement to take place.

The power to heat the SMA plates can be provided percutaneously by a DC/AC external power supply. A transcutaneous energy transmission system (TETS) was used to supply power to the AS. This system consisted of two coils, one outside the body (primary coil) and the other inside the body (secondary coil). A temperature-responsive reed switch (TRS, TDK, TR-55B50, Tokyo, Japan) was used to prevent overheating of the AS. When an electric current of 4A at 4V was supplied, the temperature of the SMA plates immediately started to rise, and the two plates bent to form an almond shape at a temperature of 55°C with a maximal gap of 33 mm between the plates. When the electric current was removed, the SMA plates recovered their initial shapes on natural cooling, resulting in closure of the intestines once again (Fig. 1).

Implantation of the artificial anal sphincter

The animals were placed on a surgical table in the lateral position under general anesthesia and were prepped and draped in sterile fashion. Anesthesia applied by halothane inhalation via a respirator was maintained throughout the procedure.

The creation of end-colostomy on the abdomen through the oblique muscles and the implantation of the artificial SMA anal sphincter were performed. The artificial anal sphincter and overheating protector were implanted between the peritoneum and abdominal wall. The colostomy was reached via an extraperitoneal approach and a space around it was created. The artificial anal sphincter was attached to the intestine with latches. The secondary coil

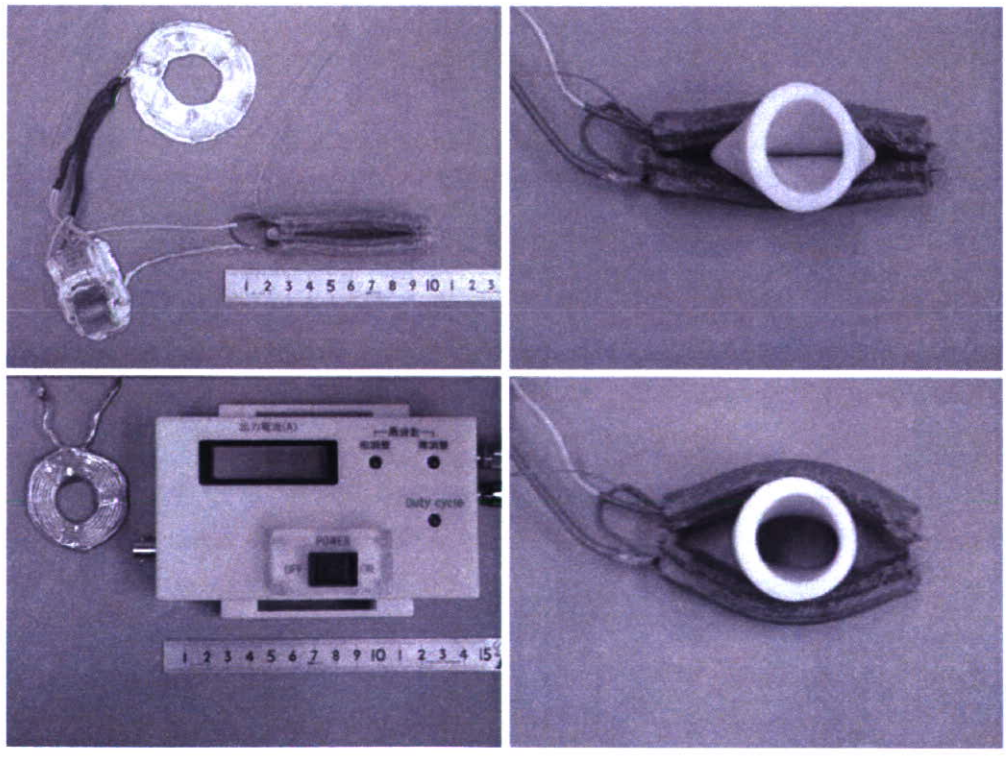

Fig. 1. Implantable components and transcutaneous energy transmission system of a shape memory alloy (SMA) artificial sphincter (AS). *Top left*, implanted components; *bottom left*, extracorporeal components; *top right*, closed state; *bottom right*, open state

was placed in the subcutaneous space near the colostomy, and the primary coil was attached to the skin, aligned with the secondary coil (Fig. 2). The lines to supply electric current to the device were led outside through a subcutaneous tunnel. An antibiotic was administrated intravenously for 3 days after surgery, and feeding was started on the day after the surgery. The bowels of the goats were moved 10 times a day by supplying electricity to the primary coil for 10 min.

Test of biocompatibility

Blood was collected from the jugular vein on days 1 and 4; at weeks 1 and 2; and at months 1, 2, and 3, postoperatively. The blood was centrifuged at 3000 rpm for 10 min to obtain the blood components from the supernatant for hematological examinations. Biochemical parameters including total protein, albumin, total bilirubin, aspartate aminotransferase (AST), blood urea nitrogen, creatinine, and C-reactive protein (CRP) were examined. The animals were killed 3 months after surgery under anesthesia, and tissue samples were collected from the intestine, liver, and kidneys and were preserved in 10% formalin.

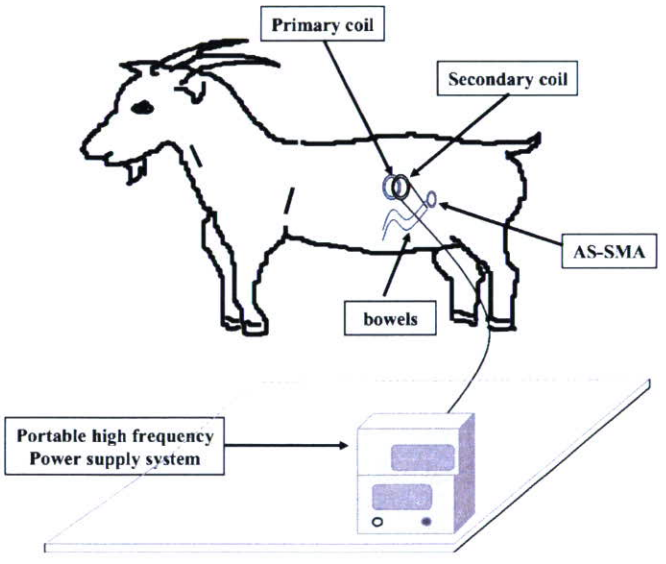

Fig. 2. Chronic animal experiment of a goat implanted with the AS-SMA

Results

In this study, the duration of the three long-term implants of the artificial anal sphincter (i.e., more than 1 week) ranged from 30 to 90 days. The data at 3 months from two of the goats could be recorded; however, the third goat was eliminated from the trial one month after the procedure due to failure of the electrodes.

The device was operated 300 times in 1 month; bowel movements were observed and the stools appeared the same as those seen before implantation. The stoma was always continent in the resting position of the AS, and the goats had a good appetite with no abdominal distension. Macroscopically, the stoma had a ruddy complexion and exhibited elasticity; there was no stricture of the intestine where the AS was attached.

Throughout the study period, the major biochemistry parameters were almost always within the normal ranges. The time courses of total bilirubin and AST of the three goats were within the baseline levels after 1 week of implantation and remained normal, indicating that there were no liver function complications (Fig. 3). The blood urea nitrogen and creatinine levels of the three goats remained within the normal range, demonstrating no renal function complications (Fig. 4). The total protein and albumin levels fluctuated within the normal ranges throughout the study period (Fig. 5), and in these goats, we also found that the level of CRP had not increased during the study.

The developed SMA artificial sphincter (AS-SMA) was implanted in animal models for chronic experiments of up to 3 months duration and exhibited good performance in maintaining fecal continence.

Discussion

The normal biochemistry results observed throughout this study bodes well for the future clinical use of the AS-SMA. Different hematological parameters were evaluated for in vivo assessment of biochemistry. The effects of the AS-SMA on renal and liver functions were evaluated by changes in total creatinine, blood urea nitrogen, bilirubin, and AST. In one goat, abnormal AST and bilirubin levels were evident on postoperative day 4, but these had returned to the normal range by postoperative day 7. The use of halothane anes-

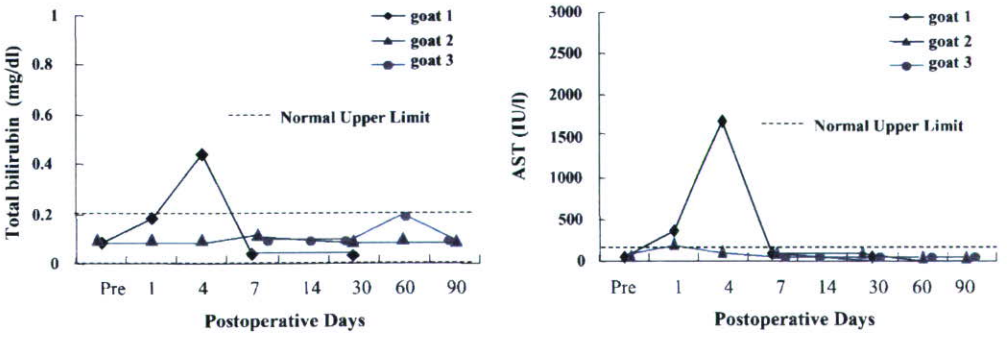

Fig. 3. Total bilirubin and aspartate aminotransferase (*AST*) levels as markers of liver function

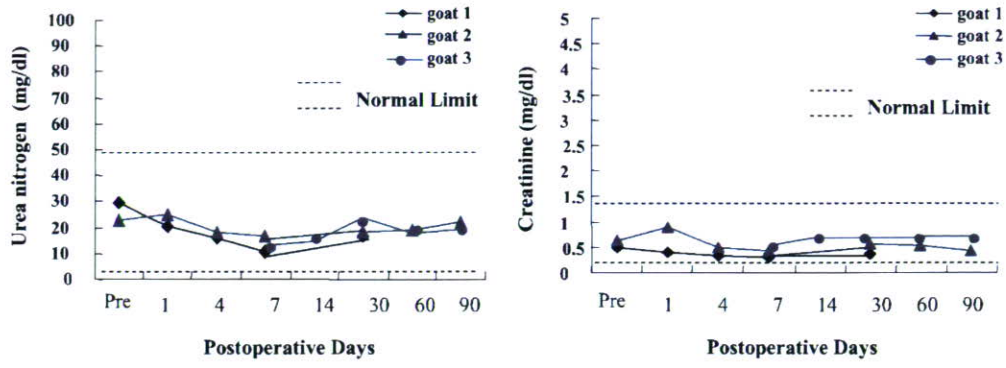

Fig. 4. Urea nitrogen and creatinine levels as markers of renal function

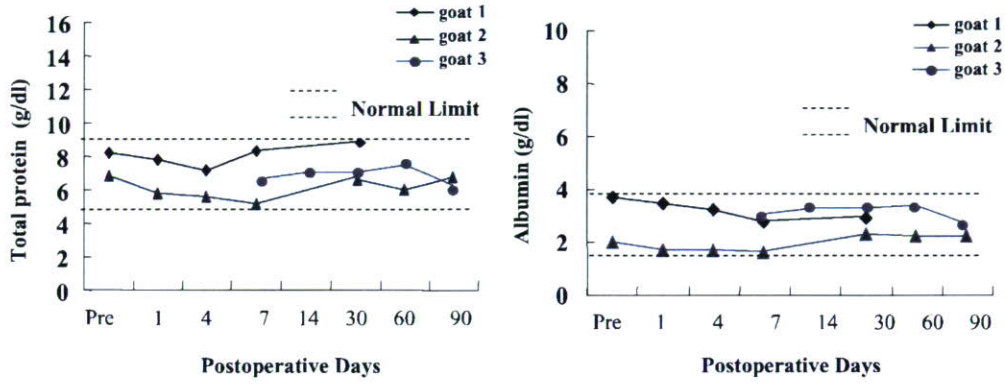

Fig. 5. Total protein and albumin levels as markers of nourishment state

thesia can induce an elevation of serum activities of liver enzymes, often around 2 to 7 days after anesthesia, and the leakage of enzyme into the serum may have come from muscle damage at the time of surgery.

Chronic in vivo studies of the AS-SMA in three goats demonstrated little influence on blood serum chemistry and showed the reliability and effective performance of the system. There were no incidences of bleeding, systemic organ dysfunction, or mechanical failure in any of the goats. Of the three long-term implanted goats, one goat was terminated after 30 days because of electrode-related issues, and two goats were terminated after 90 days. The failure of the electrodes was consistent with moisture permeation; device-related difficulties were limited to just two cable-related issues.[6–12]

Use of this AS-SMA will minimize the surgical invasiveness and compression of the surrounding tissues such as the skin and gastrointestinal system, resulting in a rapid recovery from the surgery and reduced risks of pocket bleeding, wound infection, and malnutrition. Ni-Ti alloys have been reported to exhibit good biocompatibility due to their high corrosion resistance and Ni-Ti alloys have gained popularity in the biomedical field because of their appealing mechanical properties.[11,13–15] The SMA was covered with a silicone pillow and exhibited conformity with the living body in the contact point with the anal canal. The soft silicone pillow covering material reduces the pressure concentration on the contacting area of the intestines and allows good circulation.

In this study, the small loss of power by the TETS resulted in sufficient capability for energy transmission. During the experiment, the AS opened each time energy was transmitted; however, if the efficiency were improved, less AC power would be required. The AS was kept open for 10 min, although the surface temperature was lower than 43°C because the allowable body temperature was around 42°C. The overheating protector was able to prevent burns around the AS and extended the duration of AS opening.[1,4,5]

The AS was opened for a long enough period (10 min) to allow controlled fecal continence. Fecal movements were regularly observed when the artificial anal sphincter was activated, and the evacuated feces were confirmed as being normal.

These biochemistry studies support the concept and design of this implantable artificial anal sphincter. In conclusion, this artificial anal sphincter demonstrated no adverse influence on blood serum chemistry and exhibited an effective system performance.

Acknowledgments This research was supported by the Industrial Technology Research Grant Program in 2000 (00A45027) from the New Energy and Industrial Technology Development Organization (NEDO) of Japan.

References

1. Nishi K, Kamiyama T, Wada M, Amae S, Ishii T, Takagi T, Luo Y, Okuyama T, Yambe T, Hayashi Y, Ohi R. Development of an implantable artificial anal sphincter using a shape memory alloy. J Pediatr Surg 2004;39:69–72
2. Hajivassiliou CA, Carter KB, Finlay IG. Biomechanical evaluation of an artificial anal sphincter prosthesis. J Med Eng Technol 1997;21:89–95

3. Amae S, Wada M, Luo Y, Nakamura H, Yoshida S, Kamiyama T, Yambe T, Takagi T, Nitta S, Ohi R. Development of an implantable artificial anal sphincter by the use of a shape memory alloy. ASAIO J 2001;47:346–350
4. Luo Y, Higa M, Amae S, Takagi T, Yambe T, Okuyama T, Tanaka H, Kakubari Y, Matsuki H. Preclinical development of SMA artificial anal sphincters. Minim Invasive Ther Allied Technol 2006; 15:241–245
5. Luo Y, Takagi T, Okuyama T, Amae S, Wada M, Nishi K, Kamiyama T, Yambe T, Matsuki H. Functional evaluation of an artificial anal sphincter using shape memory alloys. ASAIO J 2004;50: 338–343
6. Jain A, Mohanka R, Orloff M, Abt P, Kashyap R, Cullen J, Lansing K, Bozorgzadeh A. University of Wisconsin versus histidine-tryptophan-ketoglutarate for tissue preservation in live-donor liver transplantation. Exp Clin Transplant 2006;4:451–457
7. Mussivand T, Harasaki H, Litwak K, Slaughter MS, Gray LA Jr, Dowling TR, Mueller R, Masters RG, Hendry PJ, Beck-Da-silva L, Davies R, Haddad H, Mesana TG, Keon WJ. In vivo evaluation of the biocompatibility of the totally implantable ventricular assist device (HeartSaver VAD). ASAIO J 2003;49:459–462
8. Ortiz H, Armendariz P, DeMiguel M, Ruiz MD, Alos R, Roig JV. Complications and functional outcome following artificial anal sphincter implantation. Br J Surg 2002;89:877–881
9. Petrou SP, Elliott DS. Artificial urethral sphincter for incontinence in adults. Drugs Today (Barc) 2001;37:237–244
10. Schenk S, Weber S, Luangphakdy V, Flick CR, Chen JF, Inoue M, Kopcak MW Jr, Ootaki Y, Doi K, Dessoffy R, Hirschman GB, Vitale NG, Chapman PA Jr, Smith WA, Fukamachi K. In vivo performance and biocompatibility of the MagScrew ventricular assist device. ASAIO J 2003;49:594–598
11. Vaizey CJ, Kamm MA, Gold DM, Bartram CI, Halligan S, Nicholls RJ. Clinical, physiological, and radiological study of a new purpose-designed artificial bowel sphincter. Lancet 1998;352:105–109
12. Yokus B, Cakir DU, Kanay Z, Gulten T, Uysal E. Effects of seasonal and physiological variations on the serum chemistry, vitamins and thyroid hormone concentrations in sheep. J Vet Med A Physiol Pathol Clin Med 2006;53:271–276
13. Es-Souni M, Es-Souni M, Fischer-Brandies H. On the transformation behaviour, mechanical properties and biocompatibility of two NiTi-based shape memory alloys: NiTi42 and NiTi42Cu7. Biomaterials 2001;22:2153–2161
14. Thierry B, Tabrizian M, Trepanier C, Savadogo O, Yahia L. Effect of surface treatment and sterilization processes on the corrosion behavior of NiTi shape memory alloy. J Biomed Mater Res 2000; 51:685–693
15. Wilson SK, Delk JR II. Ectopic placement of AMS 800 urinary control system pressure-regulating balloon. Urology 2005;65: 167–170

B-mode and C-mode Imaging of Regenerated 3D Skin Model with 100 MHz Ultrasound

Yoshifumi Saijo
Department of Medical Engineering and Cardiology
Institute of Development, Aging and Cancer, Tohoku University
Sendai, Japan

Yoshihiro Hagiwara
Department of Orthopedic Surgery
Tohoku University School of Medicine
Sendai, Japan

Kazuto Kobayashi, Nagaya Okada
Honda Electronics Co. Ltd.
Toyohashi, Japan

Akira Tanaka
Faculty of Symbiotic Systems Science
Fukushima University
Fukushima, Japan

Naohiro Hozumi
Department of Electrical Engineering
Aichi Institute of Technology
Toyota, Japan

Kenji Tomihata
Gunze Co. Ltd.
Kyoto, Japan

***Abstract*—Regenerated skin with 3D structure is desired for the treatment of large burn and for the plastic surgery. High frequency ultrasound is suitable for non-destructive testing of the skin model because it provides information on morphology and mechanical properties. An acoustic microscope system capable of imaging B-mode and C-mode was developed for analysis of 3D skin model. C-mode imaging provided quantitative values of attenuation and sound speed. B-mode imaging showed fine structure of the model. Sound speed in C-mode and intensity in B-mode imaging showed higher values at the area of dense fibroblasts. The system can be used as the nondestructive evaluation tool in the process of producing 3D skin model and as the in vivo imaging system after transplantation.**

Keywords-component; 3D skin model; acoustic microscopy; B-mode; C-mode

I. INTRODUCTION

A. Current Status of Regenerated Skin

Three-dimensionally regenerated skin with epidermis, dermis, hair follicle, lipid gland and capillary is desired for the treatment of large burn or for plastic surgery. Not only the structure, should the skin model be flexible as normal skin.

Artificial dermis, Pelnac® (Gunze, Kyoto, Japan) was commercialized in Japan in 1996 [1]. Pelnac consisted of collagen sponge covered with silicon film. As it needed autologous epidermis coverage, repeated operation was required.

Cultured epidermis was approved in Japan on October 3, 2007 for orphan use of severe skin burn. Skin biopsy from the patient is performed to obtain autologous epidermis and keratinocytes are isolated from the tissue. Cells are cultured to form sheet structure and finally the sheeted epidermis is transplanted to the patient. As the epidermis is autologous, risk of rejection is avoided [2]. However, the cultured epidermis is only grown in the skin with dermis. Then it cannot be used in the case of severe burn without dermis.

Cultured dermis has the same structure as artificial dermis. Fibroblasts are cultured in the collagen sponge layer of the artificial dermis. The model was slightly advanced from the artificial dermis but it still needed autologous epidermis coverage.

Apligraf® (Organogenesis Inc., Canton, MA, USA) is bi-layered skin substitute consisting of living cells and structural proteins. The lower dermal layer combines bovine type 1 collagen and human fibroblasts (dermal cells), which produce additional matrix proteins. The upper epidermal layer is formed by promoting human keratinocytes (epidermal cells) first to multiply and then to differentiate to replicate the architecture of the human epidermis [3].

Another cultured 3D skin model, Vitrolife-Skin® (Gunze, Kyoto, Japan) is 3D human skin model used as an alternative for animal skin during irritation test. Keratinocytes are cultured to cover cultured epidermis to form two-layered structure [4].

Fig. 1 shows the schematic illustration of each regenerated skin model.

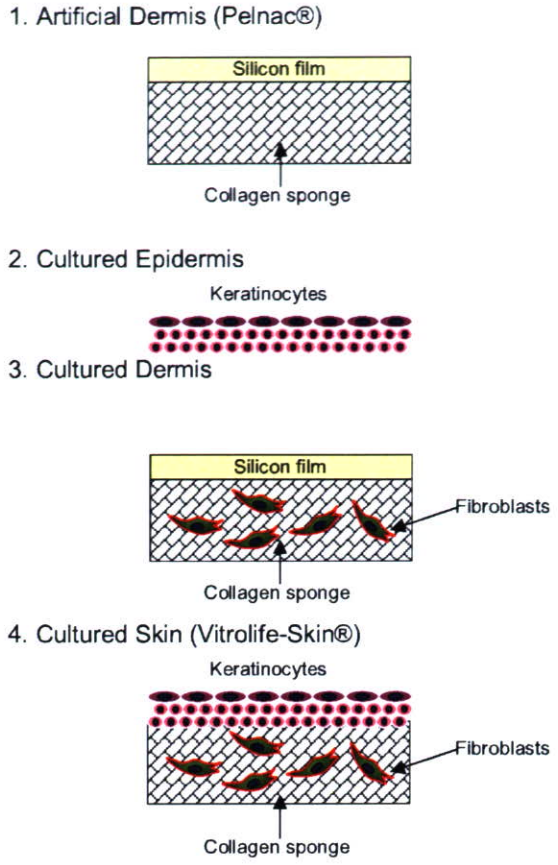

Fig. 1 Schematic illustrations of regenerated skin models

Although these cultured skins have bi-layered structure, they do not contain melanocytes, Langerhans' cells, macrophages, and lymphocytes, or other structures such as blood vessels, hair follicles or sweat glands. As they don't have vasculature, barrier function against bacterial infection is very weak. Their elastic property is different from normal skin because they are lacking elastic fiber.

B. Research and Development of Three-dimensional Complex Organ Structures

The three-dimensional molding methods and noninvasive evaluation techniques are fully employed to realize structures that are morphologically and functionally similar to those of a living body. This will enable the realization of large-size structures, regeneration of organ structures suitable to anatomical morphology, and functional reconstruction by applying various engineering techniques that are difficult to produce with present tissue engineering. At the same time, revascularization in the host site, which is necessary for achieving graft adhesion and self-organization of the three-dimensional complex organ structures, will be realized.

As a part of this research project, 3D skin model with bi-layer structure, elastic fiber and vasculature is aimed and non-invasive repetitive evaluation method is desired. High frequency ultrasound is suitable for non-destructive testing of the skin model because it provides information on morphology and mechanical properties. In the present study, the same plane, which was perpendicular to the skin surface, of the skin model with 3D structure was investigated with both B-mode and C-mode ultrasound imaging using 100 MHz ultrasound.

II. METHOD

A. System Setup

Fig. 2 shows the schematic illustration of the B-mode and C-mode imaging system. An electric impulse was generated by a high speed switching semiconductor. The start of the pulse was within 400 ps, the pulse width was 2 ns, and the pulse voltage was 40 V. The frequency of the impulse covered up to 500 MHz. The electric pulse was used to excite a PVDF transducer with the central frequency of 100 MHz. The ultrasound spectrum of the reflected ultrasound was broad enough to cover 50-160 MHz (-6dB). The reflections from the tissue was received by the transducer and were introduced into a Windows-based PC (Pentium D, 3.0 GHz, 2GB RAM, 250GB HDD) via a high-speed A/D converter (Acqiris DP210, Geneva, Switzerland). The frequency range was 500 MHz, and the sampling rate was 2 GS/s. Eight pulse echo sequences were averaged for each scan point in order to increase the signal-to-noise-ratio. The transducer was mounted on an X-Y stage with a microcomputer board that was driven by the PC through RS232C. The Both X-scan and Y-scan were driven by linear servo motors.

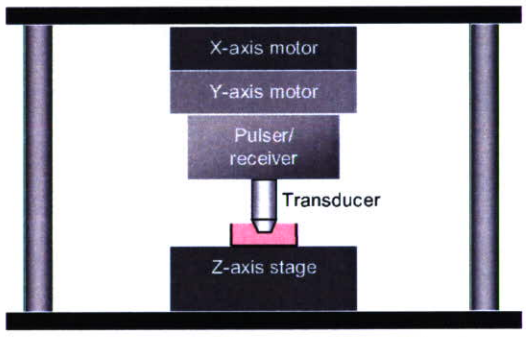

Fig. 2 Schematic illustrations of the B-mode and C-mode imaging system

B. Ultrasonic Transducers

B-mode imaging was obtained with a PVDF transducer with the diameter of 2.4 mm and the focal length of 3.2 mm. C-mode imaging was obtained with a different PVDF transducer with the diameter of 1.8 mm and the focal length of 1.5 mm.

C. Signal Processing

RF signal of each scanning line was converted to B-mode image by a conventional image processing algorithm. The scan area was 2.4 mm x 3.0 mm with 300 x 4000 pixels. Y scan width was available 8 / 16 / 24 / 64 microns step to obtain 3D data set.

The transfer function of the pulsed response at tissue region and glass region was calculated in a frequency domain to calculate the tissue thickness, attenuation and sound speed in C-mode imaging [5-7].

D. Tissue Preparation

Fibroblasts in Vitrolife-Skin were cultured with the Dulbecco's modified Eagle's medium and 10% heat-incubated bovine serum. The incubator was maintained at 37 °C and filled with 95% air and 5% CO_2.

First, B-mode images were obtained by using the saline as the coupling medium. After B-mode evaluation, the sample was frozen and sliced at 5 micron in thickness as to make the same observation plane for C-mode imaging. The neighboring sections of C-mode image were stained with Elastica-Masson staining for optical microscopic observation.

III. RESULTS

Fig. 3 shows (a) optical microscopic and (b) B-mode images of Vitrolife-Skin. Epidermis (E) was observed as a relatively high echoic band by B-mode imaging. Dermis consisted of collagen sponge and fibroblasts had heterogenic echo pattern.

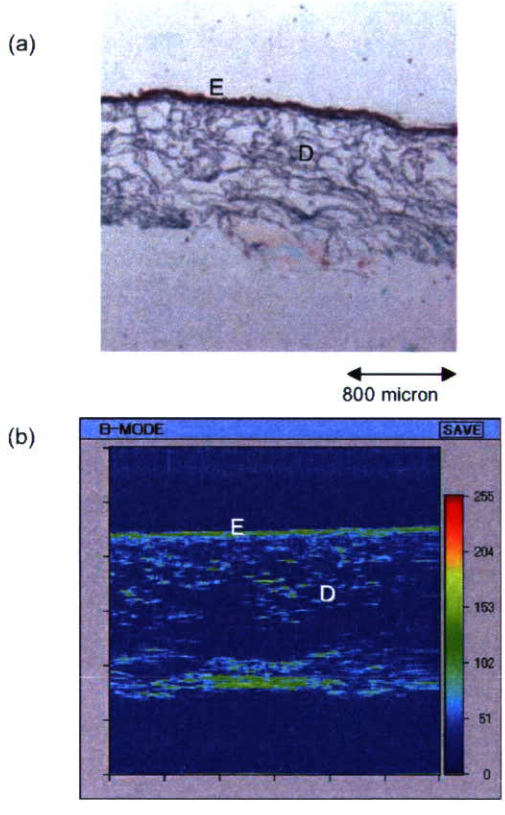

Fig. 3 (a) optical microscopic and (b) B-mode images of Vitrolife-Skin

Fig. 4 shows the (a) optical microscopic and C-mode images ((b): attenuation, (c): sound speed) of Vitrolife-Skin. The sound speed of the epidermis was approximately 1580 m/sand the sound speed of dermis was ranged 1530 to 1560 m/s corresponding to the density of fibroblasts in the dermis.

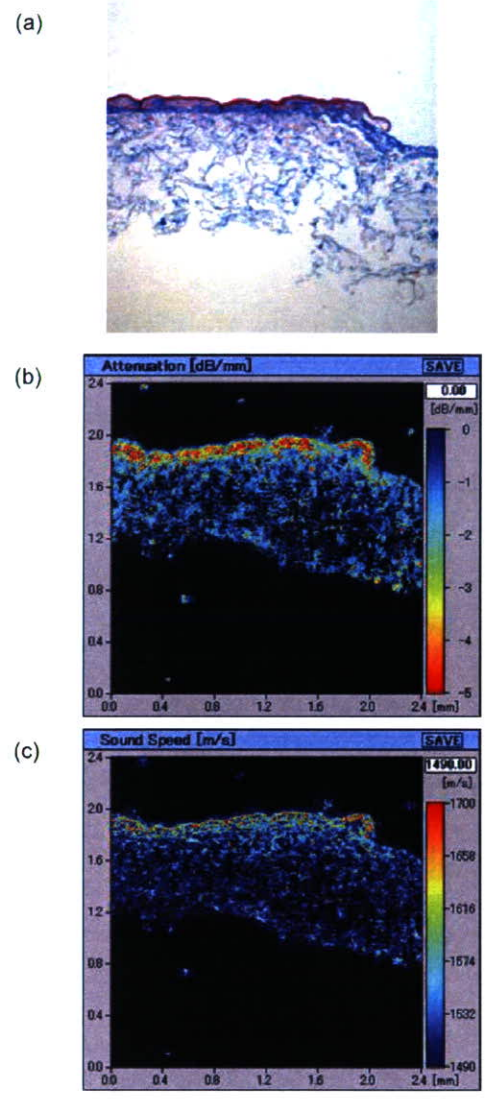

Fig. 4 (a) optical microscopic and C-mode ((b): attenuation, (c): sound speed) images of Vitrolife-Skin

The density of fibroblast (number / 0.2x0.2 mm) and the sound speed of the corresponding region were measured in 12 regions from 6 specimens. Fig. 5 shows the relationship between tow parameters. The result suggests there is a strong relationship between cellularities and sound speed.

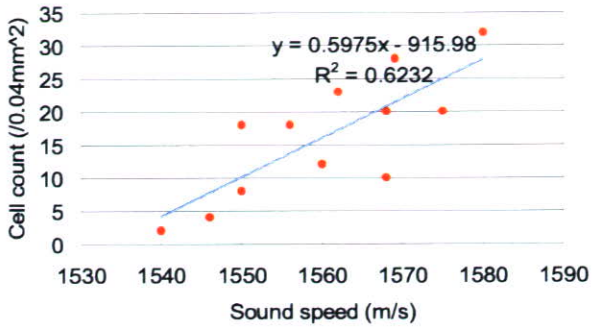

Fig. 5 Relationship between cell count and sound speed

IV. Discussion

Compared with conventional high frequency B-mode imaging modalities, this system is unique because it can be used as C-mode acoustic microscopy. C-mode quantitative values are important for understanding *in vivo* B-mode images. As the spatial resolution of the system is 15 micron, it is enough to visualize epidermis with 50-100 micron thickness. However, dermis consisting of collagen sponge and fibroblasts was hard to visualize in case the cellularties was very sparse.

One of the future directions of this imaging modality is nondestructive testing of the regenerated skin during tissue culture because it can clearly visualize the cellular density in the dermis and because non-invasive, non-contact, non-infectious method is desired for evaluation of skins. It also has a promising future as a medical imaging device. Continuous evaluation during culture and after transplantation can be performed by the same imaging system in the regenerative medicine. It can be used as a diagnostic device in dermatology. As the system clearly shows the thickness of epidermis and mechanical properties represented acoustic parameters, the system is applicable in cosmetic care of skin.

V. Conclusion

Regenerated skin with 3D structure is desired for the treatment of large burn and for the plastic surgery. High frequency ultrasound is suitable for non-destructive testing of the skin model because it provides information on morphology and mechanical properties. An acoustic microscope system capable of imaging B-mode and C-mode was developed for analysis of 3D skin model. C-mode imaging provided quantitative values of attenuation and sound speed. B-mode imaging showed fine structure of the model. Sound speed in C-mode and intensity in B-mode imaging showed higher values at the area of dense fibroblasts. The system can be used as the nondestructive evaluation tool in the process of producing 3D skin model and as the in vivo imaging system after transplantation.

Acknowledgment

This work was supported in part by Research Grants from the Ministry of Health, Labor and Welfare for the Research on Advanced Medical Technology (H17-Nano-001), Grants-in-Aid for Scientific Research (Scientific Research (B) 19300179) from the Japan Society for the Promotion of Science and Grants from New Energy and Industrial Technology Development Organization (06001905-0).

References

[1] S. Suzuki, K. Kawai, F. Ashoori, N. Morimoto, Y. Nishimura, Y. Ikada, "Long-term follow-up study of artificial dermis composed of outer silicone layer and inner collagen sponge," Br. J. Plast. Surg. Vol. 53, pp. 659-66, December 2000.

[2] K. Hata, "Current issues regarding skin substitutes using living cells as industrial materials," J. Artif. Organs, vol. 10, pp. 129-32, 2007.

[3] W.H. Eaglstein, V. Falanga, "Tissue engineering and the development of Apligraf, a human skin equivalent," Clin. Ther. Vol. 19, pp.894-905, September-October 1997.

[4] T. Uchino, H. Tokunaga, H. Onodera, M. Ando, "Effect of squalene monohydroperoxide on cytotoxicity and cytokine release in a three-dimensional human skin model and human epidermal keratinocytes," Biol. Pharm. Bull, vol. 25, pp.605-10, May 2002.

[5] N. Hozumi, R. Yamashita, C.K. Lee, M. Nagao, K. Kobayashi, Y. Saijo, M. Tanaka, N. Tanaka, S. Ohtsuki, "Time-frequency analysis for pulse driven ultrasonic microscopy for biological tissue characterization," Ultrasonics. vol. 42, pp.717-22, April 2004.

[6] Y. Saijo, N. Hozumi, C. Lee, M. Nagao, K. Kobayashi, N. Oakada, N .Tanaka, E.D. Santos Filho, H. Sasaki, M. Tanaka, T. Yambe, "Ultrasonic speed microscopy for imaging of coronary artery," Ultrasonics, vol. 44, pp.e51-5, December 2006.

[7] Y. Saijo, E. Santos Filho, H. Sasaki, T. Yambe, M. Tanaka, N. Hozumi, K. Kobayashi, N. Okada, "Ultrasonic tissue characterization of atherosclerosis by a speed-of-sound microscanning system," IEEE Trans Ultrason. Ferroelectr. Freq. Control, vol. 54, pp.1571-7, August 2007.

Precise Calibration for Biological Acoustic Impedance Microscope

N.Hozumi, A Nakano
Aichi Institute of Technology
Toyota, Japan
hozumi@aitech.ac.jp

S. Terauchi, M. Nagao, S. Yoshida
Toyohashi University of Technology
Toyohashi, Japan

K. Kobayashi
Honda Electronics Co., Ltd.
Toyohashi, Japan

S. Yamamoto
Hamamatsu University School of Medicine
Hamamatsu , Japan

Y. Saijo
Tohoku University
Sendai, Japan

***Abstract*— This report deals with the scanning acoustic microscope for imaging cross sectional acoustic impedance of biological soft tissues. A focused acoustic beam with a wide frequency range up to about 100 MHz was transmitted to the tissue object in contact with the "rear surface" of plastic substrate. The reflected signals from the target and reference are interpreted into local acoustic impedance. Two-dimensional profile is obtained by scanning the transducer. As the incidence is not vertical, not only longitudinal wave but also transversal wave is generated in the substrate. The error in estimated acoustic impedance assuming vertical incidence was discussed. The error is not negligible if the angle of focusing is large, or the acoustic impedance of the reference material is far different from the target. However it can be compensated, if the beam pattern and acoustic parameters of coupling medium and substrate were known. The improvement of precision brought by the compensation was ensured by using a droplet of saline solution of which acoustic impedance was known. Finally, a cerebellum tissue of rat was observed with a good precision.**

Keywords: biological tissue; acoustic impedanc; micro-scale imaging.

I. INTRODUCTION

In most optical microscopic observation of biological tissue, the specimen is sliced into several micrometers in thickness, and fixed on a glass substrate. The microscopy is obtained by transmitted light through the specimen. As it is normally not easy to have a good contrast by local difference in refraction and/or transmission spectrum, the specimen is usually stained before being observed. It can be classified as a kind of chemical imaging, since only a portion that has a specific chemical property can be stained by selecting an appropriate staining material. However, the staining has some disadvantages. It normally takes several hours to several days to finish the process. Furthermore, the tissue, after being stained, often completely loses its biological functions. For this reason, observation with staining process is chemically destructive.

On the other hand, acoustic micro-imaging can be performed without staining process. In this sense it is chemically non-destructive. The observation can be finished in a very short time, as it does not need the staining process. It is considered to become a powerful tool for tissue characterization that can image elastic parameters. Most of ultrasonic microscopes are scanning type, in which the response to a focused acoustic signal is successively acquired while the beam is mechanically scanned [1-4]. The authors have recently proposed the acoustic impedance microscope that can image local distribution of cross sectional acoustic impedance of soft tissues [5,6]. In this report, its methodology and improvement for establishing precision of measurement will be described. As an specimen for observation, cerebellar tissue of a rat was observed.

II. SYSTEM SETUP

Fig. 1 illustrates the outline of the acoustic impedance microscope. Distilled water was used as the coupling medium between the substrate and transducer. The transducer was PVDF-TrFE type. It was 2.4 mm in aperture diameter, and 3.2 mm in focal length, its angle of focusing being 22 deg. The acoustic wave, being focused on the interface between the substrate and tissue, was transmitted and received by the same transducer. The acoustic pulse had a wide frequency range from 10 to 100 MHz. Two-dimensional profile of acoustic im-

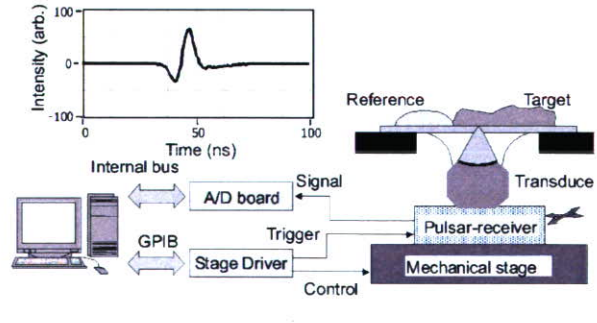

Fig. 1. Schematic diagram of the measurement system and acoustic waveform reflected from the target.

pedance was obtained by mechanically scanning the transducer using the stage driver, maintaining the focal point on the "rear surface" of the substrate. A typical field of view of 2 mm x 2 mm was covered with 200 x 200 pixels. It took typically 1 - 1.5 minutes for one observation. All the measurements were performed at room temperature.

III. Calibration Assuming Vertical Incidence

As shown in Fig. 2, the signal reflected from the target is compared with that reflected from the reference material. If the incident angle can be approximated to be perpendicular to the substrate, the target signal compared with the reference signal is interpreted into acoustic impedance as;

$$Z_{tgt} = \frac{1+\frac{S_{tgt}}{S_0}}{1-\frac{S_{tgt}}{S_0}} \cdot Z_{sub} = \frac{1-\frac{S_{tgt}}{S_{ref}} \cdot \frac{Z_{sub}-Z_{ref}}{Z_{sub}+Z_{ref}}}{1+\frac{S_{tgt}}{S_{ref}} \cdot \frac{Z_{sub}-Z_{ref}}{Z_{sub}+Z_{ref}}} \cdot Z_{sub} \quad (1),$$

where S_0 is the transmitted signal, S_{tgt} and S_{ref} are reflections from the target and reference, Z_{tgt}, Z_{ref} and Z_{sub} are the acoustic impedances of the target, reference and substrate, respectively [5]. As for the substrate, polystyrene dish (Z_{sub} =2.46 MNs/m^3) with 0.8 mm in thickness was chosen, and as for the reference material, either distilled water (Z_{ref} =1.49 MNs/m^3) or air (Z_{ref} =0.4 kNs/m^3) was employed.

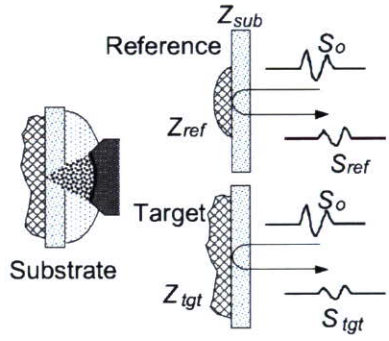

Fig. 2. Illustration for calibration of the acoustic impedance.

IV. Oblique Incidence

The estimation of acoustic impedance based on eq.(1) assumes that a plane wave is transmitted onto the target, although in fact the acoustic beam has a finite angle of focusing as shown in Fig. 3. The apparent reflection constant at the target may be different from that calculated by eq. (1), when the angle of focusing is large. In addition, when the incident angle is not zero, a part of longitudinal wave may be converted into transversal wave. This may bring an additional error in estimation of the acoustic impedance. For these reasons, error estimation was performed.

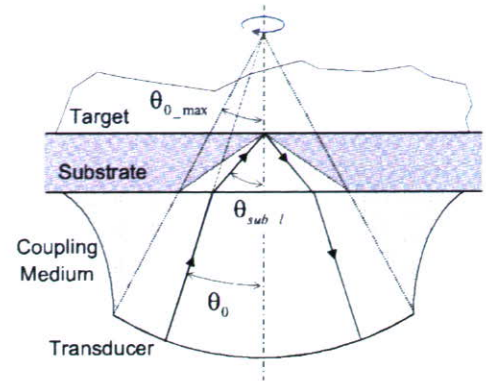

Fig. 3. Illustration of focused acoustic beam.

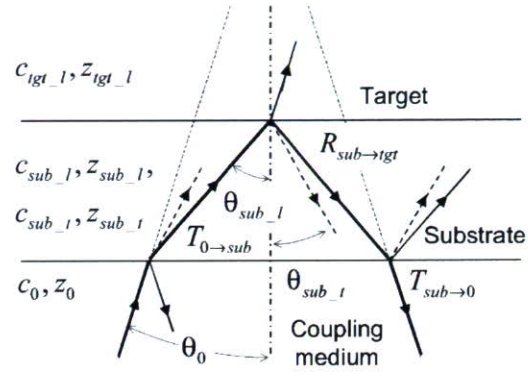

Fig. 4. Propagation of the acoustic wave with an incident angle θ_0. Solid and broken lines represent longitudinal and transversal waves, respectively. Z and c represent acoustic impedance and sound speed. l and t in the suffix indicate longitudinal and transversal waves.

Figure 4 illustrates the propagation of an acoustic wave with an incident angle of θ_0. The direction of the longitudinal wave propagating through the substrate obeys the Snell's law as;

$$\theta_{sub\_l}(\theta_0) = \sin^{-1}\left(\frac{c_{sub\_l}}{c_0}\sin\theta_0\right) \quad (2).$$

As is seen in the figure, three transversal waves are generated before the echo comes back to the transducer. These affect the apparent reflectance, however, as their sound speed is different from that of the longitudinal wave, they are not received in the limited width of the time-window.

In this report, it is assumed that transversal wave can propagate neither in the soft tissue nor the reference material. Subsequently, on the "rear surface", three modes of waves, transmitted longitudinal, reflected longitudinal and reflected transversal, are generated by the incident longitudinal wave. The reflection constant (ratio of reflected longitudinal and incident longitudinal) at the "rear surface" is represented as;

$$R_{sub\to tgt}(Z_{sub\_l}, c_{sub\_l}, c_{sub\_t}, Z_{tgt}, c_{tgt}, \theta_0)$$

$$= \frac{M_{sub} - \cos^2(2\theta_{sub\_t}) + N_{sub\to tgt}}{M_{sub} + \cos^2(2\theta_{sub\_t}) + N_{sub\to tgt}}$$

$$\theta_{sub\_t} = \sin^{-1}\left(\frac{c_{sub\_t}}{c_{sub\_l}} \sin\theta_{sub\_l}\right),$$

$$M_{sub} = \left(\frac{c_{sub\_t}}{c_{sub\_l}}\right)^2 \sin\theta_{sub\_t} \sin\theta_{sub\_l},$$

$$N_{sub\to tgt} = \frac{Z_{tgt} \cos\theta_{sub\_l}}{Z_{sub\_l} \cos\theta_{tgt}},$$

$$\theta_{tgt} = \sin^{-1}\left(\frac{c_{tgt}}{c_{sub\_l}} \sin\theta_{sub\_l}\right) \quad (3).$$

Transmission of the longitudinal wave through the "front surface" takes place twice, and affects the apparent reflection constant as;

$$T_{0\to sub} \cdot T_{sub\to 0} = T'_{0\to sub}(Z_0, c_0, Z_{sub\_l}, c_{sub\_l}, c_{sub\_t}, \theta_0)$$

$$= \frac{4N_{0\to sub}\cos^2(2\theta_{sub\_t})}{\left\{M_{sub} + \cos^2(2\theta_{sub\_t}) + N_{0\to sub}\right\}^2}$$

$$N_{0\to sub} = \frac{Z_0 \cos\theta_{sub\_l}}{Z_{sub\_l} \cos\theta_0} \quad (4).$$

Assuming that the aberration is negligible, the apparent reflection constant (ratio of received and sent waves) is described as;

$$S_{tgt}(Z_{tgt}, c_{tgt}, \theta_{0\_max}) / S_0$$

$$= \frac{\int_0^{\theta_{0\_max}} 2\pi L^2 \sin\theta_0 R_{sub\to tgt}(\theta_0) T'_{0\to sub}(\theta_0) d\theta_0}{\int_0^{\theta_{0\_max}} 2\pi L^2 \sin\theta_0 d\theta_0} \quad (5),$$

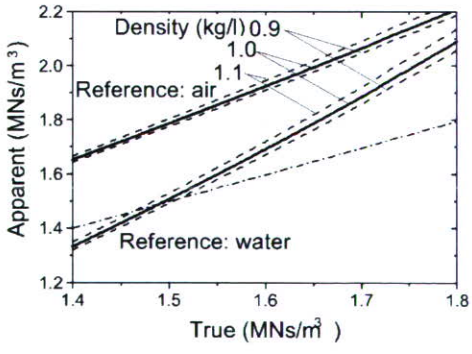

Fig. 5. Relation between true and apparent values of acoustic impedance. Angle of focusing: 22 deg. Z_{sub_l}=2.46 MNs/m^3, c_{sub_l}=2.34 km/s, c_{sub_t}=1.15 km/s.

where L is the focal length in the coupling medium.

The reflected signal from the reference material is calculated in the same manner as $S_{ref}(Z_{ref}, c_{ref}, \theta_{0\_max}) / S_0$. Referring to eq. (1), the apparent acoustic impedance assuming vertical incidence is estimated as;

$$Z_{tgt\_app} = \frac{1 + \frac{S_{tgt}(Z_{tgt}, c_{tgt}, \theta_{0\_max})}{S_{ref}(Z_{ref}, c_{ref}, \theta_{0\_max})} \cdot \frac{Z_{ref} - Z_{sub\_l}}{Z_{ref} + Z_{sub\_l}}}{1 - \frac{S_{tgt}(Z_{tgt}, c_{tgt}, \theta_{0\_max})}{S_{ref}(Z_{ref}, c_{ref}, \theta_{0\_max})} \cdot \frac{Z_{ref} - Z_{sub\_l}}{Z_{ref} + Z_{sub\_l}}} \cdot Z_{sub\_l} \quad (6).$$

Figure 5 shows the relation between the "true" and "apparent" values of acoustic impedance. As the result is dependent on c_{tgt}, it is parameterized by the density, which is given by Z_{tgt} / c_{tgt}. The true and apparent values coincide when Z_{tgt}=Z_{ref} =1.49 MNs/m (calibrated by water), and the gap increases as Z_{tgt} becomes distant from Z_{ref}. Using the air as the reference brings more significant gap, as its acoustic impedance is far more distant from the tissue. As the acoustic impedance of soft tissue is distributed approximately between 1.4 and 1.7 MNs/m^3, the error gap with these conditions is not negligible. On the other hand, the apparent value does not significantly change even if the density changes from 0.9 to 1.1 kg/*l*, in which the value of soft tissues is distributed.

V. Conpensation

The apparent acoustic impedance calibrated by using eq. (1) can be compensated by the curves shown in Fig. 5. In order to ensure the improvement of precision brought by the above compensation, droplets of saline solution were observed. The acoustic impedance of these droplets were once estimated by

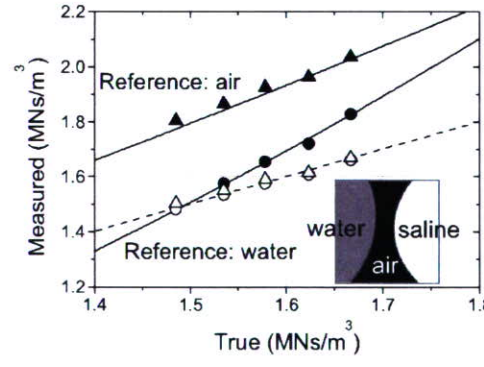

Fig. 6. Result of measurement for droplets of saline solution. True value, corresponding to salinity, is taken from the database. Filled plots indicate values as calibrated assuming vertical incidence, and open plots indicate values after the compensation considering oblique incidence. Solid lines correspond to those in Fig. 5. Angle of focusing: 22 deg. Z_{sub_l}=2.46 MNs/m^3, c_{sub_l}=2.34 km/s, c_{sub_t}=1.15 km/s. Assumed density: 1.0 kg/*l*.

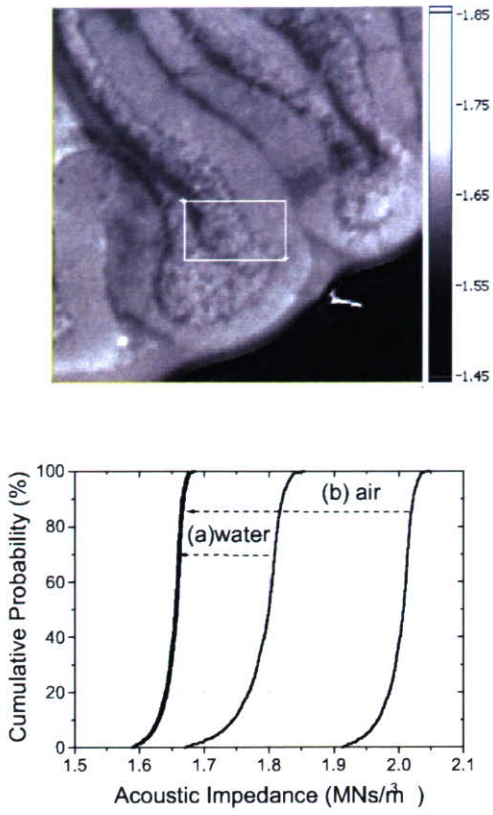

Fig. 7. Acoustic impedance micro-image of a cerebellar tissue of a rat (indicated in MNs/m^3, 2 mm x 2 mm) and cumulative probability of acoustic impedance in the region indicated as the white square, before and after the compensation: (a) calibrated by distilled water (Z_{ref}=1.49 MNs/m^3, c_{ref}=1.49 km/s), (b) calibrated by air (Z_{ref}=0.4 kNs/m^3, c_{ref}=0.34 km/s).

assuming vertical incidence, using either distilled water or the air as a reference. As the acoustic impedance of these saline droplets depending on salinity is known, these values were assumed to be the "true" values. As shown in Fig. 6, the measured value depends on the reference material and whether or not the compensation is performed. It is seen that the calibrated values assuming vertical incidence agree with the "apparent values" in Fig. 5. The value calibrated by air is more distant from the true value. The value calibrated by water is the same as the true value when the target is identical to the reference, and becomes more distant from the true value as the target becomes more different from the reference. The values after the compensation is very close to the true value, not depending on the reference material.

The acoustic impedance image of a cerebellar tissue of a rat shown in Fig. 7 was obtained after the compensation. In this report, the density was approximated to be 1.0 kg/*l*. Note that the tissue was chemically fixed using formaldehyde, so the value might be a bit higher than the fresh one. The graph for cumulative probability in Fig. 7 shows the distribution of acoustic impedance in the region surrounded by the white square in the micro-image. The compensated value is distributed between 1.59 and 1.68 MNs/m^3, regardless of the reference material. Before the compensation, it used to be distributed between 1.68 and 1.85 MNs/m^3 when calibrated by distilled water, and between 1.92 and 2.04 MNs/m^3 when calibrated by air. The result that the distributions after the compensation agree quit well suggests the adequacy of the compensation.

VI. Conclusions

Acoustic impedance microscope for biological soft tissues is proposed. Cross-sectional profile of the acoustic impedance of the tissue is obtained by mechanically scanning the transducer. The value calibrated assuming vertical incidence was considered to have non-negligible error when the angle of focusing was as large as 22 deg. The error, however, can be compensated by calculating reflection and transmission coefficients depending on the incident angle of each wave component. The observation of cerebellum tissue of a rat proved the adequacy of the compensation.

Acknowledgements

This study was financially supported by Grants-in-Aid for Scientific Research, and Japan Society for the Promotion of Science and Health and Labor Sciences Research Grants from the Ministry of Health, Labor and Welfare for the Research on Advanced Medical Technology.

References

[1] Y. Saijo, M. Tanaka, H. Okawai, H. Sasaki, S. Nitta & F. Dunn: "Ultrasonic Tissue Characterization of Infarcted Myocadium by Scanning Acoustic Microscopy", *Ultrasound in Med. & Biol.*, 23-1, 77 (1997).

[2] H. Okawai, K Kobayashi & S. Nitta: "An Approach to Acoustic Properties of Biological Tissues Using Acoustic Microgfraphs of Attenuation Constant and Sound Speed", *J. Ultrasound Med.*, 20, 891 (2001).

[3] N. Hozumi, R. Yamashita, C-K Lee, M. Nagao, K. Kobayashi, Y. Saijo, M. Tanaka, N. Tanaka & S Ohtsuki: "Ultrasonic Sound Speed Microscope for Biological Tissue Characterization Driven by Nanosecond Pulse", *Acoustic Science & Technology*, 24, 386 (2003).

[4] N. Hozumi, R. Yamashita, C-K. Lee, M. Nagao, K. Kobayashi, Y. Saijo, M. Tanaka, N. Tanaka & S.Ohtsuki: "Time –frequency analysis for pulse driven ultrasonic microscopy for biological tissue characterization", *Ultrasonics*, 42, 717 (2003).

[5] N. Hozumi, A. Kimura, S. Terauchi, M. Nagao, S. Yoshida, K. Kobayashi & Y. Saijo: "Acoustic Impedance Micro-imaging for Biological Tissue Using a Focused Acoustic Pluse with a Frequency Range Up to 100 MHz", *Proc. IEEE International Ultrasonics Symposium*, 170-173 (2005).

[6] A. Kimura, N. Hozumi, S. Terauchi, M. Nagao, S. Yoshida, K. Kobayashi & Y. Saijo: "Development of Cerebella Tissue of Rat Characterized by Acoustic Impedance Microscope", *Proc. IEEE International Ultrasonics Symposium*, 423-426 (2006).

The American Journal of Pathology, Vol. 171, No. 4, October 2007

DOI: 10.2353/ajpath.2007.061191

Cardiovascular, Pulmonary and Renal Pathology

Macrophage Colony-Stimulating Factor Improves Cardiac Function after Ischemic Injury by Inducing Vascular Endothelial Growth Factor Production and Survival of Cardiomyocytes

Tatsuma Okazaki,* Satoru Ebihara,* Masanori Asada,* Shinsuke Yamanda,* Yoshifumi Saijo,† Yasuyuki Shiraishi,† Takae Ebihara,* Kaijun Niu,* He Mei,* Hiroyuki Arai,* and Tomoyuki Yambe†

From the Department of Geriatrics and Gerontology, Tohoku University School of Medicine, Sendai; and the Department of Medical Engineering and Cardiology,† Institute of Development, Aging, and Cancer, Tohoku University, Sendai, Japan*

Macrophage colony-stimulating factor (M-CSF), known as a hematopoietic growth factor, induces vascular endothelial growth factor (VEGF) production from skeletal muscles. However, the effects of M-CSF on cardiomyocytes have not been reported. Here, we show M-CSF increases VEGF production from cardiomyocytes, protects cardiomyocytes and myotubes from cell death, and improves cardiac function after ischemic injury. In mice, M-CSF increased VEGF production in hearts and in freshly isolated cardiomyocytes, which showed M-CSF receptor expression. In rat cell line H9c2 cardiomyocytes and myotubes, M-CSF induced VEGF production via the Akt signaling pathway, and M-CSF pretreatment protected these cells from H_2O_2-induced cell death. M-CSF activated Akt and extracellular signal-regulated kinase signaling pathways and up-regulated downstream anti-apoptotic Bcl-xL expression in these cells. Using goats as a large animal model of myocardial infarction, we found that M-CSF treatment after the onset of myocardial infarction by permanent coronary artery ligation promoted angiogenesis in ischemic hearts but did not reduce the infarct area. M-CSF pretreatment of the goat myocardial infarction model by coronary artery occlusion-reperfusion improved cardiac function, as assessed by hemodynamic parameters and echocardiography. These results suggest M-CSF might be a novel therapeutic agent for ischemic heart disease. *(Am J Pathol 2007, 171:1093–1103; DOI: 10.2353/ajpath.2007.061191)*

The administration of angiogenic growth factors such as vascular endothelial growth factor (VEGF) is an innovative strategy to treat myocardial ischemia. VEGF has been used in animal models and in clinical trials of myocardial ischemia to develop growth of collateral blood vessels and to promote myocardial perfusion, and its therapeutic potential has been reported.[1–3] Hematopoietic growth factors are potent therapeutic agents for myocardial infarction. Erythropoietin improved cardiac function after myocardial infarction.[4,5] Granulocyte colony-stimulating factor (G-CSF) improved cardiac function and prevented cardiac remodeling after myocardial infarction.[6] A combination of stem cell factor and G-CSF treatment improved cardiac function and survival after myocardial infarction.[7] Macrophage colony-stimulating factor (M-CSF) in combination with G-CSF improved ventricular function after myocardial infarction in rats, but few results were shown by M-CSF treatment alone, and their mechanism was not defined.[8] Moreover, to estimate growth factor-induced therapeutic angiogenesis in hearts, large animal models are necessary,[3] but the effects of M-CSF in large animal models have not been reported. M-CSF has been initially characterized as a hematopoietic growth factor, and has been used to prevent severe infections in myelosuppressed patients after cancer chemotherapy.[9,10] M-CSF stimulates the survival, prolifera-

Supported by the Ministry of Education, Science, and Culture (grants 15590795, 18014004, 17590777, and 18790528); the Ministry of Health, Labor, and Welfare of the Japanese Government (Grant for Longevity Science grants 16C-1 and 18C-7); and by the Program for Promotion of Fundamental Studies in Health Science of Organizing for Drug ADR Relief, R&D Promotion, and Product Review of Japan.

Accepted for publication June 27, 2007.

Current address of T.O.: Department of Anatomy, University of California-San Francisco, San Francisco, CA.

Address reprint requests to Satoru Ebihara, M.D., Ph.D., Department of Geriatrics and Gerontology, Tohoku University School of Medicine, Seiryo-machi 1-1, Aoba-ku, Sendai 980-8574, Japan. E-mail: s_ebihara@geriat.med.tohoku.ac.jp.

tion, and differentiation of cells from mononuclear phagocyte lineage.[11]

Expression of VEGF in the heart has been documented,[12,13] and cardiomyocytes have been reported as a major source of VEGF in the heart.[12] Skeletal muscles expressed VEGF,[13,14] and M-CSF increased VEGF production from skeletal muscles *in vivo* and *in vitro*,[14] but it is unknown whether M-CSF increases VEGF production from cardiomyocytes. M-CSF treatment increased serum VEGF levels in mice,[14] and the level was in the potentially therapeutic range that could treat ischemic diseases in human patients.[15]

Erythropoietin and G-CSF directly protected cardiomyocytes from cell death stimulation.[4,6] M-CSF improves the survival of mononuclear phagocyte lineage cells,[11] but the cell survival effect of M-CSF on cardiomyocytes is unknown. As for their signaling pathways, M-CSF activates Akt, extracellular signal-regulated kinase (ERK), and/or Janus-associated kinase (Jak)-signal transducer and activator of transcription (STAT) cell signaling pathways in bone marrow-derived macrophages and macrophage cell lines.[16–18] M-CSF increased VEGF production in skeletal muscles via Akt activation *in vitro*.[14] However, the cell signaling pathways of M-CSF in cardiomyocytes have not been investigated.

In the present study, we investigated the angiogenic and protective effects of M-CSF on cardiomyocytes *in vitro* and *in vivo*, in mice, rats, and goats. We show that M-CSF increases VEGF production in cardiomyocytes via Akt activation, directly protects cultured cardiomyocytes and myotubes from cell death stimulation by Akt and ERK activation and by up-regulation of downstream anti-apoptotic protein Bcl-xL. Moreover, we show the benefits of M-CSF treatment for ischemic heart diseases *in vivo* using goats as a large animal model.

Materials and Methods

Reagents and Cell Culture

Human M-CSF (Kyowa Hakko Kogyo, Tokyo, Japan) was dissolved in saline for goat experiments described below or in phosphate-buffered saline (PBS) for other experiments. Phycoerythrin-labeled anti-M-CSF receptor (M-CSF-R) monoclonal antibody, control rat IgG2a, and unlabeled anti-CD16/32 monoclonal antibody were purchased from eBioscience (San Diego, CA). H9c2 cells (American Type Culture Collection, Manassas, VA) were cultured in high-glucose Dulbecco's modified Eagle's medium containing 10% fetal calf serum, 100 U/ml penicillin, and 0.1 mg/ml streptomycin (growth medium, GM). To induce cardiac differentiation, H9c2 myoblasts were cultured in differentiation medium (DM) with daily supplementation of 10 nmol/L *all-trans*-retinoic acid (ATRA) (Sigma, St. Louis, MO), with medium changed every 2 days.[19] The difference between GM and DM is 1% fetal calf serum in DM. H9c2 myoblasts were differentiated to myotubes by culturing in the same DM for 11 days.[20] Mouse primary cardiomyocytes were obtained from 1- to 3-day-old neonatal C57BL/6 mice.[21] Heart ventricles were washed in ice-cold Hanks' balanced salt solution without either Ca^{2+} or Mg^{2+} and then minced. The cells were dissociated with 0.25% trypsin in Hanks' balanced salt solution. The supernatants were collected every 15 minutes and centrifuged. To exclude nonmuscle cells, the cells were cultured at 37°C for 2 hours. Then the suspended cells were collected and cultured at 1×10^5 cells/cm^2. After 48 hours, more than 90% of the cells were considered as cardiomyocytes by cross-striation structure staining with Bodipy FL phallacidin (Molecular Probes, Eugene, OR).

Cell Proliferation and Cell Death Assays

H9c2 cells (5×10^3 cells) were plated on 96-well plates and differentiated to cardiomyocytes or myotubes, and the assays were performed as previously shown.[22] For proliferation assays, H9c2 cardiomyocytes or myotubes were treated with M-CSF for indicated time periods, and the cell numbers were counted by a water-soluble tetrazolium (WST) assay using a cell counting kit (Dojindo, Tokyo, Japan). For cell death assays, differentiated H9c2 cells were incubated with M-CSF in the presence or absence of PD98059 (at 30 or 6 μmol/L; Biosource, Camarillo, CA) or LY294002 (at 10 or 2 μmol/L; Biosource) for 24 hours. Then the cells were stimulated with indicated amount of H_2O_2 for 8 hours. The cell viability was determined by the WST assay.

Flow Cytometry

The cells were incubated with unlabeled anti-CD16/32 monoclonal antibody to block nonspecific binding and then with phycoerythrin-labeled antibodies. Flow cytometry was performed with a FACScan (BD Bioscience, San Jose, CA).[14]

Histology

The goat hearts were fixed in 10% formalin, embedded in paraffin, and sectioned. The sections were stained with hematoxylin and eosin (H&E) or Masson's elastic stain. The microvessel density in myocardial infarction lesions was determined as previously shown by immunohistochemical staining of goat hearts with polyclonal rabbit anti-human factor VIII-related antigen antibody (DakoCytomation, Carpinteria, CA) at 1:200 dilution.[14,23] The applicability of this antibody to goats was previously reported.[24] The image with the highest microvessel density was chosen at ×100 magnification, and the vessels were counted at ×200 magnification. Two independent investigators counted at least four fields for each section, and the highest count was taken. To quantify the infarct area, a standard point-counting technique was used as previously described with minor modifications.[25] In brief, the whole heart cross section with highest infarct area was selected, and a 200-point grid was superimposed onto each captured image using Adobe Photoshop (Adobe Systems Inc., San Jose, CA). The area fraction of infarction was

calculated by dividing the number of infarct points by the total number of points falling on the tissue section and was expressed as a percentage.

Western Blot Analysis

Western blot analysis was performed as shown previously.[26] H9c2 myoblasts (5×10^6 cells) were cultured in GM on day 0. From day 1, the cells were differentiated to cardiomyocytes or myotubes. After differentiation, the cells were serum-starved for 6 hours and stimulated with M-CSF. For inhibitor experiments, the cells were cultured with inhibitors for 30 minutes and then stimulated with M-CSF and inhibitors. PD98059 was incubated at a concentration of 30 or 6 μmol/L, and LY294002 was incubated at a concentration of 10 or 2 μmol/L. The cell lysates were subjected to 12% sodium dodecyl sulfate-polyacrylamide gel electrophoresis and transferred onto polyvinylidene difluoride membranes (Millipore, Billerica, MA). The membranes were blotted with antibodies to phospho-ERK, phospho-Akt, phospho-Stat1, phospho-Stat3, phospho-Bad, Bcl-xL (Cell Signaling Technology, Beverly, MA), phospho-Jak1, or M-CSF-R (Santa Cruz Biotechnology, Santa Cruz, CA). The membranes blotted with antibodies to detect phosphorylation were then reblotted with antibodies to total ERK, Akt, Stat1, Stat3, Bad (Cell Signaling Technology), or Jak1 (Santa Cruz Biotechnology).

Mouse and Goat Preparation

The Laboratory Animal Committee at Tohoku University approved all animal experiments. Male C57BL/6 mice, 7 to 9 weeks old, were injected intramuscularly with M-CSF (200 μg/kg body weight) or PBS (control) for 3 consecutive days ($n = 5$ per group). Adult male goats (48 to 53 kg body weight) were intubated and anesthetized with 2% halothane as previously reported ($n = 3$ per group).[27] The goats were incised between the fourth and fifth ribs, and a left lateral thoracotomy was performed. Myocardial infarction was induced by left anterior descending coronary artery ligation with some modifications.[28] For the permanent left anterior descending coronary artery ligation model, left anterior descending coronary artery was ligated at a point ~60% from the beginning of the left coronary artery to the apex. M-CSF (40 μg/kg body weight) intravenous injection began just after the ligation and continued daily for 13 days; on day 14, the goats were anesthetized with 2% halothane and sacrificed. Control goats were injected with saline. For the ischemia-reperfusion model, M-CSF was injected intravenously for 3 consecutive days. Then the left anterior descending coronary artery was ligated at a point ~40% from the beginning of the left coronary artery to the apex for 30 minutes followed by reperfusion.[5] A micromanometer tipped catheter (Millar Instruments Inc., Houston, TX) was positioned in the left ventricle (LV). Hemodynamic parameters were recorded using a data recording unit (TEAC Corp., Tokyo, Japan) with sampling frequency of 1.5 kHz. Echocardiography was performed using a Sonos 5500 (Hewlett Packard, Andover, MA).

Enzyme-Linked Immunosorbent Assay (ELISA)

Mouse hearts were isolated, washed, homogenized in ice-cold PBS, and centrifuged. The protein level in the supernatant was adjusted to 10 mg/ml by the BCA protein assay kit (Pierce, Rockford, IL), and subjected to ELISA using a VEGF ELISA kit (R&D Systems, Minneapolis, MN). Carrageenan (Sigma) and rat anti-mouse CD11b monoclonal antibody (Serotec, Oxford, UK) treatment was performed as previously reported.[14] Culture medium of mouse primary cardiomyocytes (2×10^5 cells) was changed daily. H9c2 myoblasts (5×10^3 cells) were differentiated to cardiomyocytes or myotubes. H9c2 cardiomyocytes were incubated with M-CSF and ATRA in the presence or absence of LY294002 (10 μmol/L) for indicated time periods with daily culture medium change. H9c2 myotubes were cultured with M-CSF for indicated time periods. All of the supernatants were assayed by ELISA.

RNA Isolation and Reverse Transcriptase-Polymerase Chain Reaction (RT-PCR)

Total RNA was isolated using RNAzol B reagent (Tel-Test, Friendswood, TX). Placenta total RNA was purchased from BD Biosciences. Quantitative RT-PCR for VEGF and conventional RT-PCR for M-CSF-R were performed as previously shown.[14]

Data Analysis

Data are presented as mean ± SD. Statistical analysis was performed using analysis of variance with Fisher's least significant difference test. P values <0.05 were considered as significant.

Results

M-CSF Increases Heart VEGF Production in Vivo

Previous studies have shown that M-CSF increased VEGF production in skeletal muscles, and the heart expresses VEGF. Therefore, we examined whether M-CSF increases heart VEGF production. Mice were treated with M-CSF, and then the cytoplasmic RNA in heart was assessed by quantitative RT-PCR. M-CSF significantly increased VEGF mRNA expression level in the hearts by 221% (Figure 1A). M-CSF receptor (M-CSF-R) mRNA expression was confirmed by conventional RT-PCR, and placenta-derived mRNA was used as a positive control (Figure 1B). To confirm VEGF at the protein level, M-CSF was injected into mice. The hearts were isolated, and ELISA for VEGF was performed. VEGF was detected in controls (Figure 1C). M-CSF significantly increased VEGF in the hearts by 21% (Figure 1C). Because M-CSF induces VEGF production *in vitro* from human monocytes,[29] we sought to clarify whether cardiomyocytes or the monocytes/macrophages in the heart produced VEGF after M-CSF treatment. Mice were treated with carra-

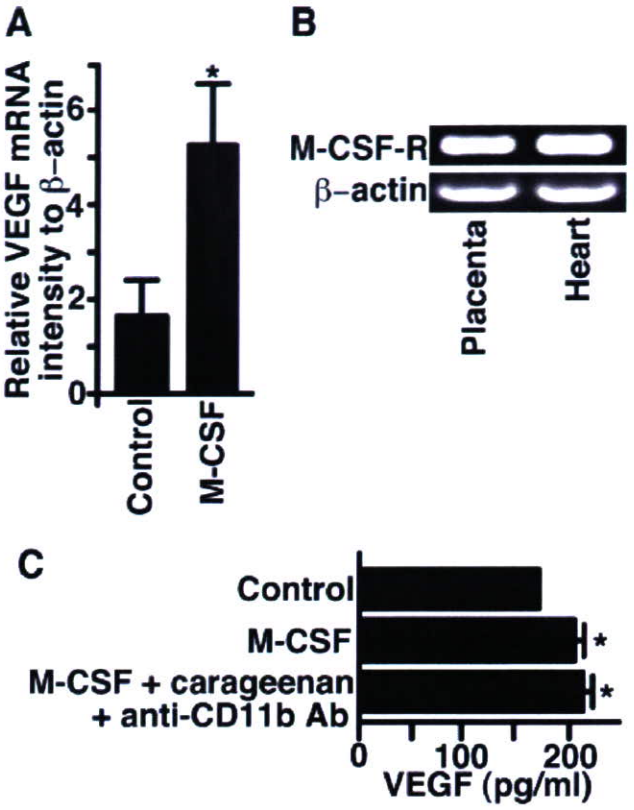

Figure 1. M-CSF increased heart VEGF production *in vivo*. Mice were injected intramuscularly with M-CSF (200 μg/kg) or PBS (control) for 3 consecutive days ($n = 5$ per group). **A:** Quantitative RT-PCR determined the VEGF mRNA expression. M-CSF treatment significantly increased the VEGF mRNA expression in hearts ($^*P < 0.05$). **B:** Conventional RT-PCR determined the M-CSF receptor (M-CSF-R) expression (top), and β-actin expression (bottom). **C:** The hearts were washed, homogenized in PBS, and centrifuged. ELISA determined the VEGF level in the supernatants containing 10 mg/ml protein. M-CSF significantly increased the VEGF level. M-CSF + carrageenan + anti-CD11b Ab indicates mice injected with carrageenin (1 mg) on days 1 and 4, with anti-CD11b monoclonal antibody (0.5 mg) on days 3 and 5, and with M-CSF on days 3, 4, and 5. On day 6, the hearts were isolated. This treatment did not affect the VEGF level ($^*P < 0.05$). Similar results were obtained from two independent experiments.

geenan and anti-CD11b monoclonal antibody to eliminate the monocytes/macrophages, as shown previously.[14] Macrophages were hardly observed in control mice hearts or in treated mice hearts (data not shown). The treatment did not affect M-CSF-induced VEGF production in the heart (Figure 1C).

M-CSF Increases VEGF Production by Cardiomyocytes in Vitro

To confirm the effect of M-CSF on heart VEGF production *in vitro*, mouse neonatal cardiomyocytes were isolated and stimulated with M-CSF. The culture medium was changed daily to maintain cell viability. Control cardiomyocytes produced VEGF, and M-CSF significantly increased the VEGF level on days 2 (by 10%) and 3 (by 31%) (Figure 2A). The M-CSF-R expression on cardiomyocytes was confirmed by fluorescence-activated cell sorting analysis (Figure 2B).

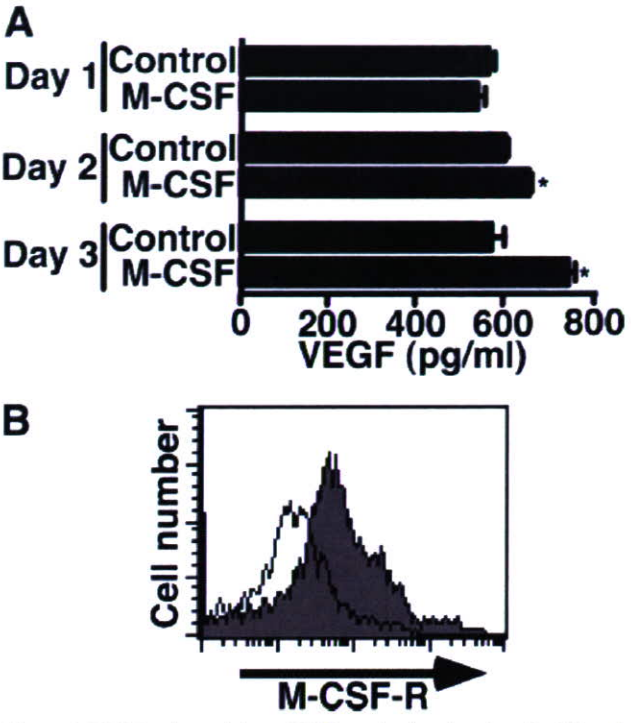

Figure 2. M-CSF enhanced heart VEGF production *in vitro*. **A:** Cultured cardiomyocytes from neonatal mice were stimulated with M-CSF (100 ng/ml) for the indicated time periods. Culture medium was changed daily, and the supernatants were subjected to ELISA. M-CSF significantly enhanced VEGF production on days 2 and 3 ($^*P < 0.01$). **B:** Cultured cardiomyocytes from neonatal mice expressed M-CSF-R. The shaded histogram indicates staining with M-CSF-R, and the blank histogram indicates background staining with control IgG. Similar results were obtained from two independent experiments.

M-CSF Increases VEGF Production from Differentiated H9c2 Cells

To investigate the effects of M-CSF on cardiomyocytes more precisely, rat H9c2 myoblast cells were differentiated to cardiomyocytes. H9c2 myoblasts differentiate to cardiomyocytes when they are cultured in DM with ATRA.[19] After differentiation, DM with ATRA was changed daily to maintain cell viability. VEGF was detected in supernatants from controls, and M-CSF increased H9c2 cardiomyocyte VEGF production on days 2 (by 10%) and 3 (by 20%) (Figure 3A). M-CSF increased skeletal muscle VEGF production.[14] H9c2 myoblasts cultured in the DM without ATRA for 11 days differentiate to H9c2 myotubes.[20] After differentiation, H9c2 myotubes were treated with M-CSF. H9c2 myotubes produced VEGF, and M-CSF significantly enhanced VEGF production on day 8 by 29% (Figure 3B).

M-CSF Protects Differentiated H9c2 Cells from H_2O_2-Induced Cell Death

Because M-CSF increased VEGF production from differentiated H9c2 cells, we investigated whether M-CSF increased the H9c2 cardiomyocyte cell number and found that it did not (Figure 4A). Similar results were obtained from the H9c2 myotubes (Figure 4A). M-CSF improves the survival of the mononuclear phagocyte lineage

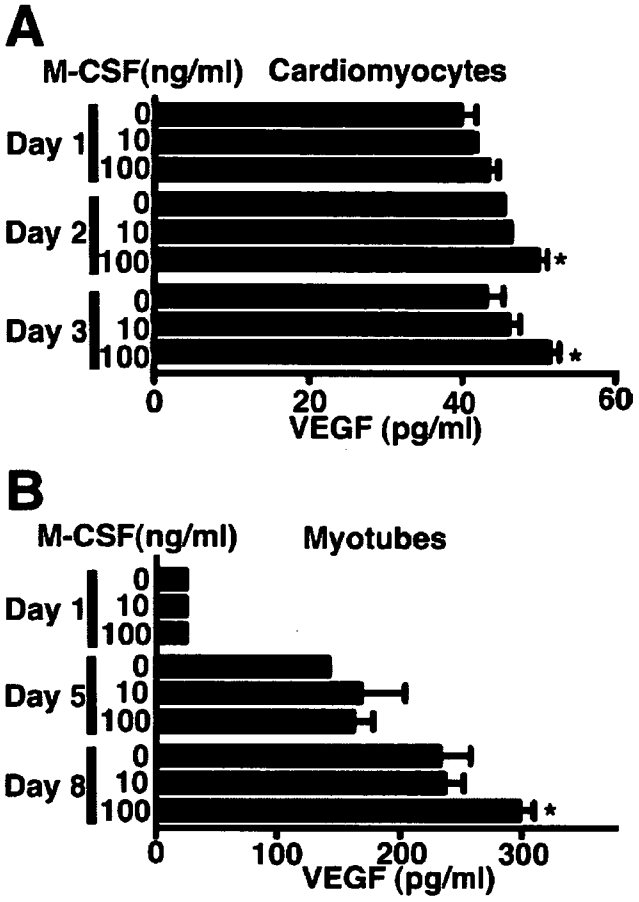

Figure 3. M-CSF increased VEGF production in differentiated H9c2 cells. **A:** H9c2 myoblasts cultured in DM (changed every 2 days) with daily supplementation of 10 nmol/L ATRA for 7 days were differentiated to H9c2 cardiomyocytes. The cells were stimulated with the indicated amount of M-CSF for indicated time periods. The culture medium was changed daily, and ELISA determined the VEGF level in the supernatant. M-CSF (100 ng/ml) increased VEGF production on days 2 and 3 ($^*P < 0.05$). **B:** H9c2 myoblasts cultured in the same DM for 11 days were differentiated to H9c2 myotubes. Then the cells were stimulated with the indicated amount of M-CSF for the indicated time periods without medium change. M-CSF (100 ng/ml) significantly increased VEGF production on day 8 ($^*P < 0.03$). Similar results were obtained from three independent experiments.

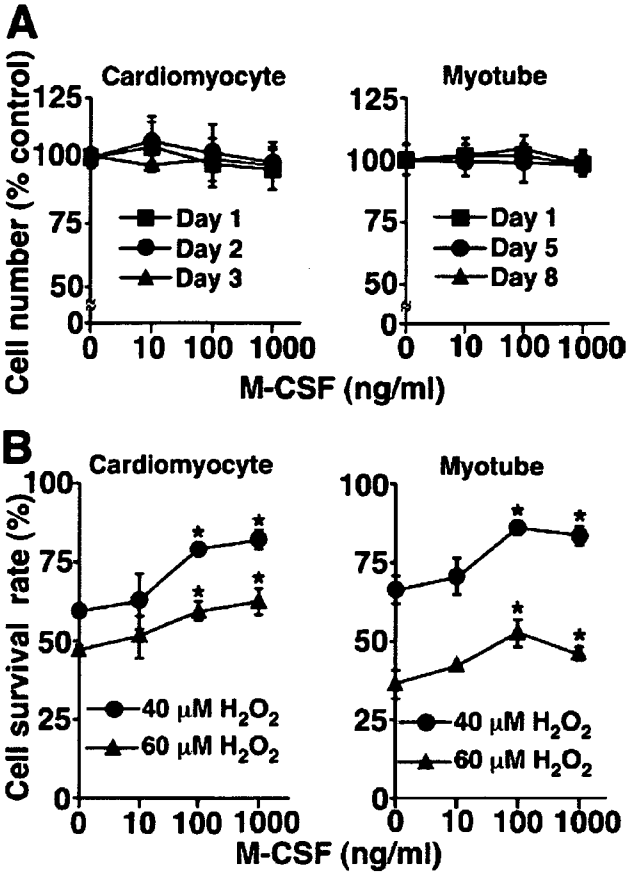

Figure 4. M-CSF protects differentiated H9c2 cells from H_2O_2-induced cell death. **A:** H9c2 cardiomyocytes were cultured with the indicated amount of M-CSF and ATRA for the indicated time periods, and the culture medium was changed daily. H9c2 myotubes were cultured with the indicated amount of M-CSF for the indicated time periods. WST assay determined the cell number. **B:** H9c2 cardiomyocytes or H9c2 myotubes were cultured with the indicated amount of M-CSF for 24 hours and then stimulated with H_2O_2 (40 or 60 μmol/L) for 8 hours. The culture medium of H9c2 cardiomyocytes was supplemented with ATRA. WST assay determined the cell viability. M-CSF (100 and 1000 ng/ml) significantly protected the cells from H_2O_2-induced cell death ($^*P < 0.03$). Similar results were obtained from three independent experiments.

cells.[11] Therefore, the cell survival effect of M-CSF on differentiated H9c2 cells from cytotoxic H_2O_2 exposure was examined. H9c2 cardiomyocytes were incubated with M-CSF and then exposed to H_2O_2. M-CSF significantly protected H9c2 cardiomyocytes from H_2O_2-induced cell death (Figure 4B). Similar results were obtained from H9c2 myotubes (Figure 4B).

M-CSF Activates ERK and Akt Signaling Pathways and Increases Bcl-xL Expression in Differentiated H9c2 Cells

The cell signaling pathways of M-CSF in cardiomyocytes and H9c2 myotubes have not been investigated. To elucidate molecular mechanisms of the M-CSF-induced cell survival, differentiated H9c2 cells were treated with M-CSF and then activation of ERK, Akt, and Jak-STAT signaling pathways was investigated. Western blot analysis showed two forms of M-CSF-R in differentiated H9c2 cells (Figure 5, A and C).[30] In H9c2 cardiomyocytes, M-CSF induced ERK activation, as indicated by its protein phosphorylation, whereas the protein levels of the total ERK in cell lysates were not different (Figure 5A). M-CSF activated the Akt, but M-CSF did not activate Jak1, Stat1, or Stat3 (Figure 5A). ERK activation protects cardiomyocytes from cell death by up-regulating the anti-apoptotic protein Bcl-xL and inactivating the apoptotic protein Bad by its phosphorylation at Ser112.[31,32] Akt activation improves cardiomyocyte survival, but the main downstream signaling pathways of Akt for cardiomyocytes survival has not been clarified.[33] To clarify the target molecules of ERK in H9c2 cardiomyocytes, Bcl-xL expression was examined. Bcl-xL was detected in cells without M-CSF stimulation (Figure 5B). M-CSF up-regulated Bcl-xL expression, which peaked at 24 and 48 hours (Figure 5B). M-CSF did not phosphorylate Bad at Ser112 (Figure 5B). These results suggest M-CSF protected H9c2 cardiomyocytes by activating Akt and up-regulating Bcl-xL expression through ERK activation. In H9c2 myotubes, M-CSF activated ERK and Akt but did not activate Jak1 or Stat3